*J. Fluid Mech.* (2021), *vol*. 918, A11, doi:10.1017/jfm.2021.349

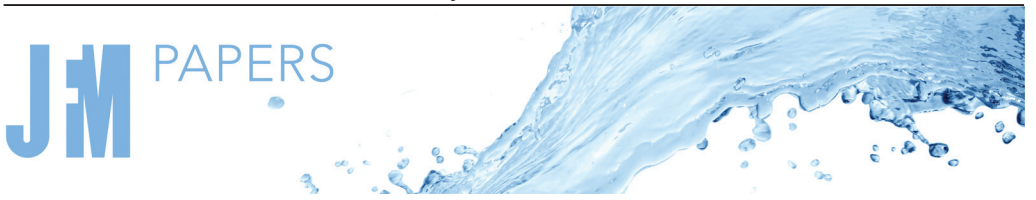


# A new linearly unstable mode in the core-annular flow of two immiscible fluids

**Kirti Chandra Sahu**†

Department of Chemical Engineering, Indian Institute of Technology Hyderabad, Sangareddy, Telangana 502 285, India

(Received 19 June 2020; revised 26 January 2021; accepted 16 April 2021)

The linear stability characteristics of pressure-driven core-annular pipe flow of two immiscible fluids are considered to investigate the effects of the density and viscosity ratios, the Reynolds number, the interface location and the interfacial tension. Both liquid–liquid and gas–liquid systems are examined. A new type of interfacial mode associated with the axisymmetric and corkscrew perturbations is discovered for certain ranges of the viscosity and density ratios in the immiscible liquid–liquid system. Two distinct unstable regions at long and short wavelengths are observed. The long-wavelength unstable region forms a close loop, indicating that it is not a Tollmien–Schlichting mode. The new interfacial mode observed in the present study is similar to that discovered by Mohammadi & Smits (*J. Fluid Mech.*, vol. 826, 2017, pp. 128–157) in two-layer Couette flow for low viscosity ratios. In contrast to the two distinct unstable regions found in the immiscible configuration, the corresponding miscible system contains only one unstable mode. It is found that, in the liquid–liquid systems, the corkscrew (axisymmetric) perturbation is dominant when the annular fluid is less (more) viscous than the core fluid. On the other hand, the axisymmetric perturbation is always the dominant one in the gas–liquid system. In gas–liquid systems, the interfacial tension stabilises the short-wave and destabilises the long-wave perturbations, while increasing the interface radius stabilises the flow due to the presence of a plug region in the pipe.

**Key words:** core-annular flow, gas/liquid flow

## 1. Introduction

Two-layer flows are commonly observed in many natural phenomena, such as magma flows, glaciers, the Earth's outer core, the ocean and atmosphere (Govindarajan & Sahu 2014) and industrial applications, such as crude oil transport in pipelines (Saffman & Taylor 1958; Joseph *et al.* 1997; Cao *et al.* 2003), coating technology (Weinstein &

† Email address for correspondence: ksahu@che.iith.ac.in

Ruschak 2004), displacement flow (Redapangu, Sahu & Vanka 2012), de-icing aircraft wings (Yih 1990) to name a few. The pioneering work by Yih (1967) demonstrated the existence of an interfacial unstable mode associated with an infinitesimal small long-wave perturbation at any Reynolds number in plane Couette and plane Poiseuille flows of two immiscible fluids with different viscosities separated by a sharp interface. Since then, several researchers have studied the interfacial instability in the long-wave limit (Hooper 1985), short-wave limit (Hooper & Boyd 1983) and also via full linear stability analysis in two-layer plane Poiseuille (Yiantsios & Higgins 1988*a*,*b*; Sahu *et al.* 2007; Valluri *et al.* 2010; Sahu & Matar 2010), Couette (Mohammadi & Smits 2017), three-layer channel (Malik & Hooper 2005; Sahu *et al.* 2007; Redapangu *et al.* 2012) and core-annular cylindrical pipe (Hickox 1971; Joseph, Renardy & Renardy 1984; Salin & Talon 2019; Usha & Sahu 2019) flows. The mechanism of the short-wave interfacial instability was provided by Hinch (1984). By conducting an energy budget analysis for the linear perturbations, Boomkamp & Miesen (1996) showed that the interfacial instability is driven by the work done at the interface due to the jump in viscosity across the interface.

Instability in the core-annular cylindrical pipe flow of two miscible (Scoffoni, Lajeunesse & Homsy 2001; Selvam *et al.* 2007, 2009; Sahu 2016, 2019) and immiscible fluids (Hickox 1971; Joseph *et al.* 1984; Salin & Talon 2019; Usha & Sahu 2019) has received increasing attention recently, not only because of its importance in many practical applications but also due to its fundamental interest. The single-fluid Hagen–Poiseuille flow is known to be linearly stable for all values of Reynolds number (Schmid & Henningson 2001), which is not true in two-fluid flows in a cylindrical pipe. The focus of all of the above investigations in core-annular cylindrical pipe flows was to demonstrate the behaviour of the linearly unstable axisymmetric and corkscrew perturbations associated with viscosity stratification (in the miscible configuration) or viscosity contrast (in the immiscible configuration) between the fluids in density matched systems. The main findings of the earlier studies in the stability of core-annular pipe flows of miscible and immiscible fluids are summarised below. (i) While the immiscible configuration is unstable if the core fluid is more viscous than the annular fluid (Joseph *et al.* 1997), the miscible configuration is found to be unstable beyond a critical viscosity ratio (Selvam *et al.* 2007). (ii) In miscible configurations, the axisymmetric perturbation is dominant when the core fluid is more viscous than the annular fluid, but when the core fluid is less viscous, the corkscrew perturbation is most dangerous (Selvam *et al.* 2007). This result is in contrast with that of the immiscible core-annular pipe flow in which the axisymmetric perturbation was found to be most unstable when the core fluid is less viscous than the annular fluid (Usha & Sahu 2019). It is also worth mentioning that in the Hagen–Poiseuille single-fluid flow (albeit stable for any Reynolds number), the corkscrew perturbation is always the least stable one (Schmid & Henningson 2001). (iii) Selvam *et al.* (2009) and Salin & Talon (2019) demonstrated the transition from the convective instability to the absolute instability in miscible and immiscible core-annular flows of two immiscible fluids of different viscosities but of the same density.

In the present work, we demonstrate the appearance of a new mode of instability distinct from the Tollmien–Schlichting (TS) mode and Yih's interfacial mode in core-annular cylindrical pipe flow of two immiscible fluids. In this context, it is important to discuss the earlier studies on the stability of two-layer plane Poiseuille flow of two miscible fluids (Ranganathan & Govindarajan 2001; Govindarajan 2004; Malik & Hooper 2005; Sahu & Govindarajan 2016) and two-layer Couette flow of two immiscible fluids (Ern, Charru & Luchini 2003; Mohammadi & Smits 2017). Ern *et al.* (2003) demonstrated that the most unstable mode in the miscible configuration is similar to that observed in immiscible flows

without surface tension for low diffusivity and in the limit of zero thickness of the mixed region. However, in the miscible configuration, they also found that, for a certain range of diffusivity and interfacial thickness, the growth rate of the perturbations is higher than the corresponding interfacial mode. In a three-layer channel flow, Govindarajan (2004) reported the existence of a linearly unstable regime distinct from the TS mode and showed that these unstable regions merged when the mixed layer overlaps with the critical layer (i.e. the location at which the perturbation phase velocity is equal to the mean streamwise velocity). By comprising the instability behaviour of two miscible and immiscible fluids in a two-layer plane Poiseuille flow, Malik & Hooper (2005) showed that when the thickness of the mixed region is comparable to the thickness of the critical layer, the most unstable mode resembles the interfacial mode (Yih 1967). In a miscible channel flow, Talon & Meiburg (2011) observed four different types of modes depending on the location of the mixed region in the Stokes flow regime. By analysing the concentration perturbation, they showed that the most unstable mode is similar to that of Ern *et al.* (2003).

Most relevant to the present study is the discovery of a new type of interfacial instability distinct from Yih's mode (Yih 1967) in a two-layer Couette flow for low viscosity ratio by Mohammadi & Smits (2017). They also investigated the influence of the density ratio and interfacial tension. In the present study, besides demonstrating the distinct interfacial mode of instability in a core-annular cylindrical pipe flow, the effect of the viscosity and density ratios is also studied, with an emphasis on investigating the linear instability in the core-annular gas–liquid system that has not yet been studied to the best of the author's knowledge. The new interfacial instability mode is compared with the most unstable mode observed in the corresponding miscible core-annular flow. Two configurations have been considered in the gas–liquid system, namely, when the annular fluid is a liquid and the core fluid is a gas, and *vice versa*. The effects of interface location and interfacial tension have also been investigated. The rest of this paper is organised as follows. The problem is formulated and the governing linear stability equations for immiscible and miscible core-annular configuration are derived in § 2. The associated boundary conditions are also presented in this section. The linear stability results are discussed in § 3. Concluding remarks are provided in § 4.

## 2. Formulation

### 2.1. *Immiscible core-annular configuration*

Linear instability characteristics of a steady and fully developed core-annular pressure-driven flow of two Newtonian and immiscible, incompressible fluids in a vertical cylindrical pipe of radius $R$ are considered. This schematic diagram is shown in figure 1. A cylindrical coordinate system $(r, \theta, z)$ is used, where $r, \theta$ and $z$ denote the radial, azimuthal and axial coordinates, respectively. The density and viscosity of the core fluid (fluid '1' in $0 \leqslant r \leqslant R_0$) and annular fluid (fluid '2' in $R_0 \leqslant r \leqslant R$) are denoted by $(\rho_1, \mu_1)$ and $(\rho_2, \mu_2)$, respectively. The interfacial tension acting at the interface separating the immiscible fluids is denoted by $\sigma$. Both liquid–liquid and gas–liquid systems are considered in this study. The flow dynamics is governed by the continuity and the Navier–Stokes equations in the cylindrical coordinate system, which are non-dimensionalised using the radius of the pipe ($R$) and average velocity ($V = Q/\pi R^2$) as the length and velocity scales, respectively. Here, $Q$ is the volumetric flow rate. In the non-dimensionalisation, the properties of fluid '1' are used as the reference scales. The reduced dimensionless pressure $p_k$ in fluid $k$ ($k = 1, 2$) is related to the corresponding total dimensional pressure, $p_{d,k}$ as

$$p_k = (p_{d,k} + \rho_k g z)/\rho_k V^2. \tag{2.1}$$

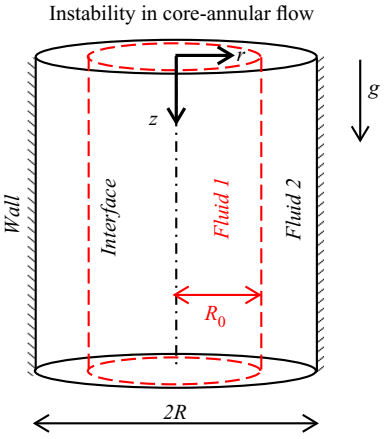


Figure 1. Schematic of the pressure-driven core-annular flow of two immiscible fluids in a vertical pipe of radius $R$. The acceleration due to gravity, $g$ acts in the positive $z$-direction. The fluids are separated by a sharp interface located at $r = R_0$.

The various dimensionless numbers are the Reynolds number, ($Re = \rho_1 VR/\mu_1$), the viscosity ratio ($\mu_r = \mu_2/\mu_1$), the density ratio ($\rho_r = \rho_2/\rho_1$), the dimensionless radius of the interface, ($R_i = R_0/R$) and the inverse capillary number, ($\Gamma = \sigma/\mu_1 V$). Here, $V$ denotes the average velocity.

### 2.1.1. *Basic state*

The basic state is a steady, parallel, fully developed unidirectional flow in the axial direction, $U_{z,k}$ in the core ($k = 1$) and annular ($k = 2$) regions of the pipe. The basic state velocity profiles in the core ($r \in [0, R_i]$) and annular ($r \in [R_i, 1]$) regions are given by

$$U_{z,1} = -\frac{\mathrm{d}P}{\mathrm{d}z}\frac{Re}{4}({R_i}^2 - r^2) - \frac{\mathrm{d}P}{\mathrm{d}z}\frac{Re}{4\mu_r}({R_i}^2 - 1), \tag{2.2}$$

$$U_{z,2} = -\frac{\mathrm{d}P}{\mathrm{d}z}\frac{Re}{4\mu_r}(1 - r^2), \tag{2.3}$$

respectively. Equations (2.2) and (2.3) are obtained using the following boundary conditions: (i) the no-slip boundary condition at the pipe wall ($r = 1$), (ii) the velocity maximum condition ($U'_{z,1} = 0$) at the centreline of the pipe ($r = 0$) and (iii) the continuity of velocities ($U_{z,1} = U_{z,2}$) and the shear stresses ($\mathrm{d}U_{z,1}/\mathrm{d}r = \mu_r\, \mathrm{d}U_{z,2}/\mathrm{d}r$) at the interface ($r = R_i$). The pressure gradient, $\mathrm{d}P/\mathrm{d}z$ (whose value is negative for flow in the positive $z$ direction) is calculated by maintaining the constant volumetric flow condition, such that dimensionless average velocity, $V = Q/2\pi \int_0^1 U_z r\, \mathrm{d}r = 1$.

### 2.1.2. *Linear stability equations*

The temporal linear stability equations for the basic flow (2.2)–(2.3) subjected to infinitesimal perturbations are discussed in this section. A normal mode analysis is used to express each flow variable as a sum of the basic state and a time-dependent perturbation

(designated by hat)

$$(u_{r,k}, u_{\theta,k}, u_{z,k}, p_i)(r, \theta, z, t) = \big(0, 0, U_{z,k}(r), P(z)\big) + (\mathrm{i}\hat{u}_{r,k}, \hat{u}_{\theta,k}, \hat{u}_{z,k}, \hat{p}_k)(r, \theta, z, t), \tag{2.4}$$

where

$$(\mathrm{i}\hat{u}_{r,k}, \hat{u}_{\theta,k}, \hat{u}_{z,k}, \hat{p}_k) = (\mathrm{i}u_{r,k}, u_{\theta,k}, u_{z,k}, p_k)(r)\exp(\mathrm{i}\,(\alpha z + \beta\theta - \alpha ct)). \tag{2.5}$$

Similarly, the perturbed interface can be represented as $R_i + r_i \exp(\mathrm{i}(\alpha z + \beta\theta - \alpha ct))$. Here, $\mathrm{i} \equiv \sqrt{-1}$, $\alpha$, $\beta$ and $c(\equiv c_r + \mathrm{i}c_i)$ are the wavenumbers in the axial and azimuthal directions (real), and the phase speed (complex) of the perturbation, respectively. The real and imaginary parts of $c$ are denoted by $c_r$ and $c_i$, respectively. Thus a given mode is temporally unstable if $c_i > 0$, stable if $c_i < 0$ and neutrally stable if $c_i = 0$. The governing temporal linear stability equations are derived using the standard approach (Schmid & Henningson 2001; Usha & Sahu 2019), i.e. by substituting the perturbations in the dimensionless continuity and Navier–Stokes equations and then subtracting the corresponding unperturbed equations followed by linearising the resulting equations. After suppressing the hat notations, the temporal linear stability equations for both the layers, $k = (1, 2)$ are given by

$$u'_{r,k} + \frac{u_{r,k}}{r} + \frac{\beta u_{\theta,k}}{r} + \alpha u_{z,k} = 0, \tag{2.6}$$

$$\rho_k\left(-\alpha c u_{r,k} + \alpha u_{r,k} U_{z,k}\right) = p'_k - \frac{\mathrm{i}\mu_k}{Re}\left[u''_{r,k} + \frac{u'_{r,k}}{r} - \left(\frac{\beta^2+1}{r^2} + \alpha^2\right)u_{r,k} - \frac{2\beta}{r^2}u_{\theta,k}\right], \tag{2.7}$$

$$\begin{aligned}&\rho_k\left(-\alpha c u_{\theta,k} + \alpha u_{\theta,k} U_{z,k}\right)\\ &\quad = -\frac{\beta p_k}{r} - \frac{\mathrm{i}\mu_k}{Re}\left[u''_{\theta,k} + \frac{u'_{\theta,k}}{r} - \left(\frac{\beta^2+1}{r^2} + \alpha^2\right)u_{\theta,k} - \frac{2\beta}{r^2}u_{r,k}\right],\end{aligned} \tag{2.8}$$

$$\rho_k\left(-\alpha c u_{z,k} + U'_{z,k} u_{r,k} + \alpha U_{z,k} u_{z,k}\right) = -\alpha p_k - \frac{\mathrm{i}\mu_k}{Re}\left[u''_{z,k} + \frac{u'_{z,k}}{r} - \left(\frac{\beta^2}{r^2} + \alpha^2\right)u_{z,k}\right], \tag{2.9}$$

where the prime denotes differentiation with respect to $r$, $\rho_k = (1, \rho_r)$ and $\mu_k = (1, \mu_r)$. Here, $k = 1, 2$ indicates the flow region. The stability equations in each layer are the same as those given in Schmid & Henningson (2001). The boundary conditions for the perturbation variables are discussed below.

At the centreline of the pipe ($r = 0$), the boundary conditions are

$$u_{r,1} = 0, \quad u_{\theta,1} = 0, \quad u'_{z,1} = 0, \quad p'_1 = 0 \quad \text{for } \beta = 0, \tag{2.10}$$

$$u_{r,1} + u_{\theta,1} = 0, \quad 2u'_{r,1} + u'_{\theta,1} = 0, \quad u_{z,1} = 0, \quad p_1 = 0, \quad \text{for } \beta = 1, \tag{2.11}$$

$$u_{r,1} = 0, \quad u_{\theta,1} = 0, \quad u_{z,1} = 0, \quad p_1 = 0, \quad \text{for } \beta \geqslant 2. \tag{2.12}$$

At the pipe wall ($r = 1$), the boundary conditions are

$$u_{r,2} = 0, \quad u_{\theta,2} = 0, \quad u_{z,2} = 0, \tag{2.13a–c}$$

for all values of $\beta$.

The tangential stress balance equations for the perturbation at $r = R_i$ in the azimuthal and axial directions are given by

$$\mu_r\left[-\beta u_{r,2} + R_i u'_{\theta,2} - u_{\theta,2}\right] + \left[\beta u_{r,1} - R_i u'_{\theta,1} + u_{\theta,1}\right] = 0, \tag{2.14}$$

and

$$\mu_r\left[-\alpha u_{r,2} + r_i U''_{z,2} + u'_{z,2}\right] = -\alpha u_{r,1} + r_i U''_{z,1} + u'_{z,1}, \tag{2.15}$$

respectively. The normal stress balance boundary condition at $r = R_i$ is given by

$$Re(p_1 - p_2) + 2\mathrm{i}\left[\mu_r u'_{r,2} - u'_{r,1}\right] = -\frac{\Gamma r_i}{R_i^2}\left[1 - \beta^2 - \alpha^2 R_i^2\right]. \tag{2.16}$$

The velocity components are also continuous at the interface ($r = R_i$), i.e.

$$u_{r,1} = u_{r,2}, \quad u_{\theta,1} = u_{\theta,2}, \quad u_{z,1} = u_{z,2}. \tag{2.17a–c}$$

The kinematic boundary condition for perturbation is given by

$$r_i = \frac{u_{r,1}}{\alpha(U_{z,1} - c)} = \frac{u_{r,2}}{\alpha(U_{z,2} - c)}. \tag{2.18}$$

Equations (2.6)–(2.9), along with the boundary conditions (2.10)–(2.18), constitute an eigenvalue problem with the eigenvalue as the frequency of the perturbation ($\omega = \alpha c$) and eigenvectors $[u_{r,k}, u_{\theta,k}, u_{z,k}, p_i]^{\mathrm{T}}$. The domains $[0, R_i]$ and $[R_i, 1]$ are discretised using the Chebyshev spectral collocation method (Canuto *et al.* 1987), and the eigenvalue problem is solved using a public domain software, LAPACK, such that for domain $[0, R_i]$

$$r_j = \frac{R_i}{2}\left[1 - \cos\left(\frac{\pi(j-1)}{N-1}\right)\right], \tag{2.19}$$

and for domain $[R_i, 1]$

$$r_j = \frac{1}{2}\left[1 + \cos\left(\frac{\pi(j-1)}{N-1}\right)\right] + \frac{R_i}{2}\left[1 - \cos\left(\frac{\pi(j-1)}{N-1}\right)\right], \tag{2.20}$$

where $r_j$ are the locations of the Chebyshev collocation points, and $N$ is the number of collocation points in each layer. The governing equations for the corresponding miscible core-annular configuration are described in Appendix A.

### 2.2. *Validation*

The linear stability solver developed for the immiscible configuration, as discussed in § 2.1, has been validated against several known results for the single-fluid flow (Schmid & Henningson 2001) and also plane Poiseuille flow configuration of two immiscible fluids (Sahu *et al.* 2007). Table 1 shows a comparison between the most unstable eigenmode obtained using the current solver with the results of Hu & Joseph (1989) for two different set of parameters. Several authors have used the results of Hu & Joseph (1989) to validate their solvers (e.g. Orazzo, Coppola & De Luca 2014). In table 1, it can be seen that the present results are in good agreement with Hu & Joseph (1989). In addition, a grid convergence test is also performed (see figure 16 in Appendix B) to ensure that the number of grids used in the present study is adequate to generate the eigenvalues accurately, at least up to five decimal places. It is found that using more than 41 grids in each layer in the case of the immiscible configuration and 81 grids in the miscible configuration are sufficient to

| Parameters | Hu & Joseph (1989) | Present |
|---|---|---|
| Set 1: $Re_c = 499.5$, $R_i = 0.9$, $\Gamma = 2$, $\mu_r = 0.05$, $\rho_r = 1$, $\alpha = 5.0$, $\beta = 0$ | $0.38425 + 0.02075$i | $0.38405 + 0.02081$i |
| Set 2: $Re_c = 37.82$, $R_i = 0.7$, $\Gamma = 0$, $\mu_r = 0.5$, $\rho_r = 1$, $\alpha = 10$, $\beta = 0$ | $0.66929 + 0.00413$i | $0.66916 + 0.00405$i |

Table 1. Comparison of the most unstable phase speed ($c$) with Hu & Joseph (1989). Here, $Re_c = \rho_1 V_c R/\mu_1$ is the Reynolds number used by Hu & Joseph (1989), where $V_c$ is the centreline velocity.

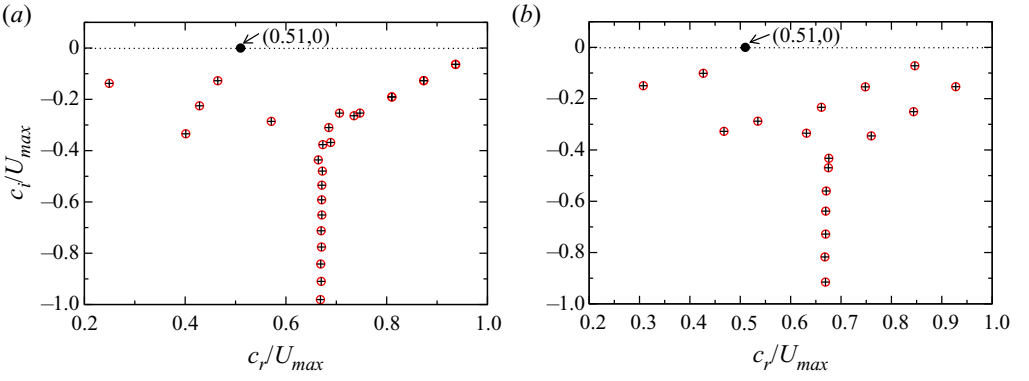


Figure 2. Comparison of the eigenvalue spectra obtained from the present simulations for the immiscible configuration with $\Gamma = 0$ ('$\circ$', red) and those given in Schmid & Henningson (2001) for the single-fluid flow through a pipe ('+'); (*a*) $\alpha = 1$, $\beta = 0$ and (*b*) $\alpha = 0.5$, $\beta = 1$. Other parameters are $Re = 1000$, $R_i = 0.7$, $\mu_r = 1$ and $\rho_r = 1$. The additional mode ('$\bullet$') obtained in the immiscible configuration (mode 'I') is a neutrally stable ($c_i = 0$) mode with $c_r = U_z|_{R_i} = 0.51 U_{max}$.

achieve the desired accuracy. Figures 2(*a*) and 2(*b*) show the comparisons of the eigenvalue spectra obtained from the present simulations for the immiscible configuration (§ 2.1) with $\Gamma = 0$ and those presented in Schmid & Henningson (2001) in the case of single-fluid flow through a pipe for ($\alpha = 1$, $\beta = 0$) and ($\alpha = 0.5$, $\beta = 1$), respectively. Other parameters are $Re = 1000$, $R_i = 0.7$, $\mu_r = 1$ and $\rho_r = 1$. The real and imaginary parts of the phase speed are normalised with the maximum velocity ($U_{max}$) of the basic state. It can be seen that all the eigenvalues are overlapped, except for one additional mode in the case of the immiscible configuration (shown by '$\bullet$'). This is a neutrally stable ($c_i = 0$) mode with $c_r = U_z|_{R_i}$, which is a solution of the kinematic boundary condition (2.18). Hereafter, this mode is termed as mode 'I'. It is observed (as also can be seen below in several figures) that mode 'I' is always present in the immiscible core-annular flow configuration (figure 1). In the following, mode 'I' will be used to distinguish the other unstable modes, namely mode '1' and mode '2', in the interfacial core-annular flow.

## 3. Results and discussion

### 3.1. *Liquid–liquid system*

In order to identify the dominant mode of the perturbation in liquid–liquid systems ($\rho_r = O(1)$), the variations of the normalised growth rate, $\alpha c_{i,max}/U_{max}$ associated with the most unstable axisymmetric ($\beta = 0$) and corkscrew ($\beta = 1$) perturbations (excluding 'I' mode) are plotted for different viscosity ratios for $\rho_r = 1.1$ and density ratios for

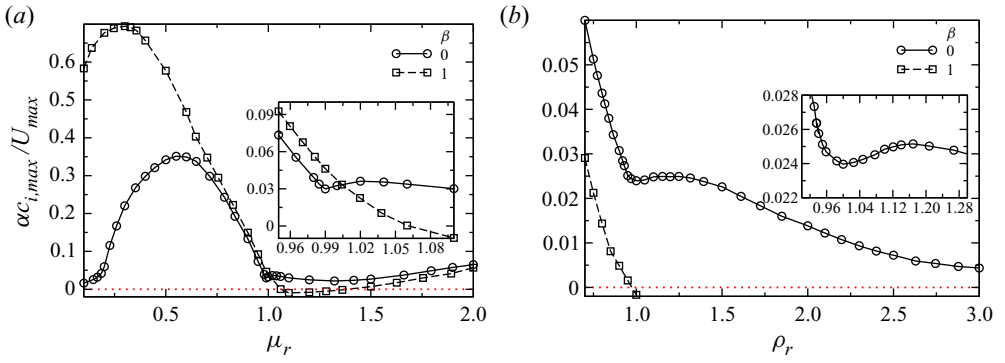


Figure 3. Effect of $\beta$ on the variations of $\alpha c_{i,max}/U_{max}$ (excluding the neutrally stable interfacial 'I' mode) with (*a*) the viscosity ratio, $\mu_r$ for $\rho_r = 1.1$, and (*b*) the density ratio, $\rho_r$ for $\mu_r = 1.2$ in the immiscible core-annular configuration. Other parameters are $Re = 1000$, $R_i = 0.7$ and $\Gamma = 0.1$. The insets in (*a*,*b*) are the magnified views near $\mu_r = 1$ and $\rho_r = 1$, respectively.

$\mu_r = 1.2$ in figures 3(*a*) and 3(*b*), respectively. Other parameters are $Re = 1000$, $R_i = 0.7$, $\Gamma = 0.1$ and $c_{i,max}$ is the phase speed of the perturbation corresponding to the most unstable wavenumber ($\alpha$) for each set of parameters. It is found (not shown) that the higher modes ($\beta \geqslant 2$) are stable for the range of parameters considered in this study. It can be seen in figure 3(*a*) that, for $\rho_r = 1.1$, while the corkscrew ($\beta = 1$) perturbation is dominant for $\mu_r < 1$ (i.e. when the annular fluid is less viscous than the core fluid), the axisymmetric ($\beta = 0$) perturbation is more unstable for $\mu_r > 1$ (i.e. when the annular fluid is more viscous than the core fluid). This is also true for other values of the density ratios, albeit for $\rho_r = O(1)$, i.e. in liquid–liquid systems, as shown in figure 3(*b*). Usha & Sahu (2019) also found that the axisymmetric perturbation is the dominant one in the core-annular flow of two immiscible fluids for $\mu_r > 1$ and $\rho_r = 1$. However, this behaviour contrasts with the miscible configuration of two isodense fluids, in which the axisymmetric perturbation is dominant for $\mu_r < 1$, but the corkscrew perturbation is more unstable for $\mu_r > 1$ (Selvam *et al.* 2007; Sahu & Govindarajan 2016).

### 3.1.1. *Axisymmetric perturbation:* $\beta = 0$

In this section, the linear instability behaviour of the axisymmetric perturbation ($\beta = 0$) in the immiscible core-annular flow is discussed. The unstable mode in the immiscible configuration is also compared with that of the corresponding miscible configuration. Figures 4(*a*) and 4(*b*) show the neutral stability curves for the most unstable mode (excluding the 'I' mode) in the $(Re, \alpha)$-plane and the variations of the normalised real part of the phase speed ($c_r/U_{max}$) along the neutral stability boundaries, respectively. The parameters used for the immiscible configuration are $R_i = 0.7$, $\Gamma = 0$, $\rho_r = 1$, $\mu_r = 0.1$ and $\beta = 0$. It can be seen in figure 4(*a*) that there are two distinct unstable regions corresponding to the long wavelengths (small $\alpha$) and short wavelengths (large $\alpha$). The normalised phase speeds of these modes are approximately 0.5 and 0.9 (see, figure 4*b*), which are termed as 'mode 1' and 'mode 2', respectively. It can also be seen that only one mode is unstable in the corresponding miscible core-annular configuration with Schmidt number, $Sc = 1$ and mixed layer thickness, $q = 0.02$ (shown by the dashed line in figure 4*a*,*b*). The value of $c_r/U_{max}$ in the miscible configuration lies in between the two unstable modes in the immiscible configuration. It is also verified that the result qualitatively remains the same even when the value of $q$ is 10 % of the pipe radius and

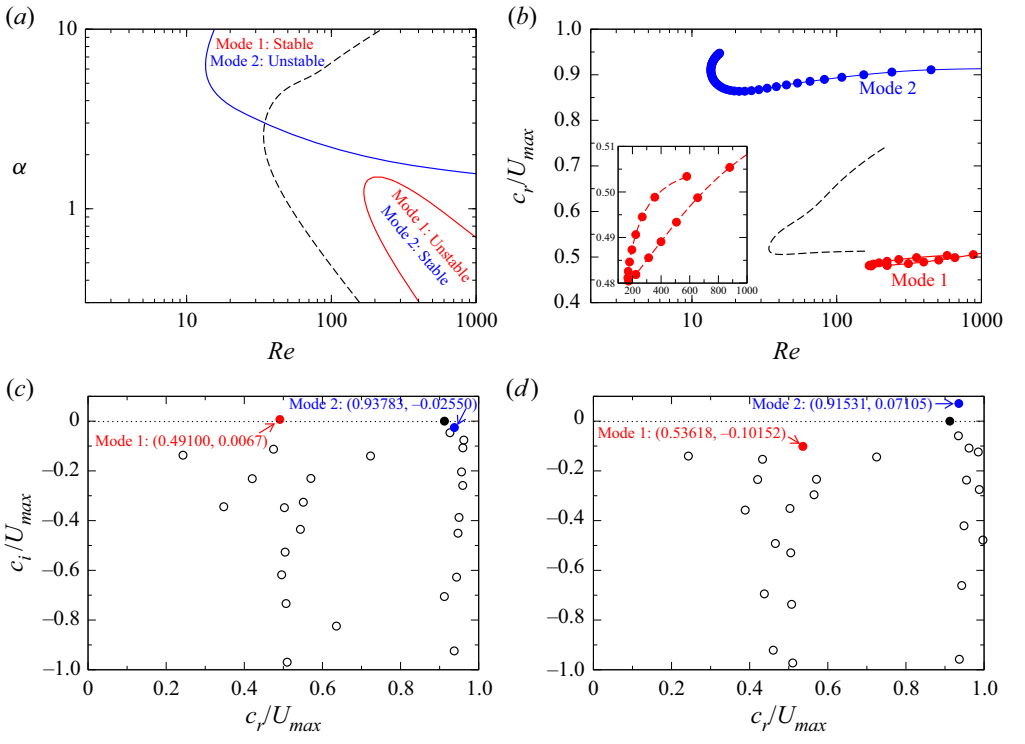


Figure 4. (*a*) The neutral stability curves corresponding to the most unstable axisymmetric ($\beta = 0$) perturbation (excluding the 'I' mode). (*b*) Variation of the real part of the phase speed of the most unstable mode as a function of *Re*. The inset in (*b*) corresponds to mode '1' in the linear scale. The result associated with the corresponding miscible configuration (with $Sc = 1$, $q = 0.02$) is shown by the black dashed line in (*a*,*b*). The eigenvalue spectra in the immiscible configuration for (*c*) $Re = 500$, $\alpha = 1$ and (*d*) $Re = 100$, $\alpha = 5$. The mode 'I' with $c_r = 0.91234$ is shown by symbol (•) in (*c*,*d*). Other parameters are $R_i = 0.7$, $\Gamma = 0$, $\rho_r = 1$ and $\mu_r = 0.1$.

for a range of finite *Sc* values (see, figure 15 in Appendix A). It is found that mode '1' in the low $\alpha$ region becomes stable at sufficiently high values of *Re*. This indicates that this mode is inviscidly stable and thus, cannot be a TS mode. Mohammadi & Smits (2017) found a similar unstable mode in two-layer Couette flow for low viscosity ratios. This point is discussed further in § 3.1.2.

The eigenvalue spectra associated with the immiscible configuration for $Re = 500$, $\alpha = 1$ (one typical set of parameters in the long-wavelength unstable region) and $Re = 100$, $\alpha = 5$ (one typical set of parameters in the short-wavelength unstable region) are shown in figures 4(*c*) and 4(*d*), respectively. It can be seen that, for $Re = 500$, $\alpha = 1$, mode '1' is unstable ($c_{r1}, c_{i1} = 0.49100, 0.0067$) and mode '2' is stable ($c_{r2}, c_{i2} = 0.93783, -0.02550$). On the other hand, for $Re = 100$, $\alpha = 5$, mode '1' becomes stable ($c_{r1}, c_{i1} = 0.53618, -0.10152$) and mode '2' is unstable ($c_{r2}, c_{i2} = 0.91531, 0.07105$). It is also observed that, for $\mu_r < 1$, while in the long-wavelength region the real part of the phase speed of the most unstable mode is smaller than that of the 'I' mode, in the short-wavelength region it is higher or of the same order.

To further understand the behaviour of the two distinct unstable modes in the immiscible configuration, the neutral stability curves are plotted for different values of the viscosity ratio in figure 5(*a–f*). The rest of the parameters are the same as those used to generate figure 4(*a*). It can be seen that, as we increase the value of $\mu_r$ (while remaining below one),

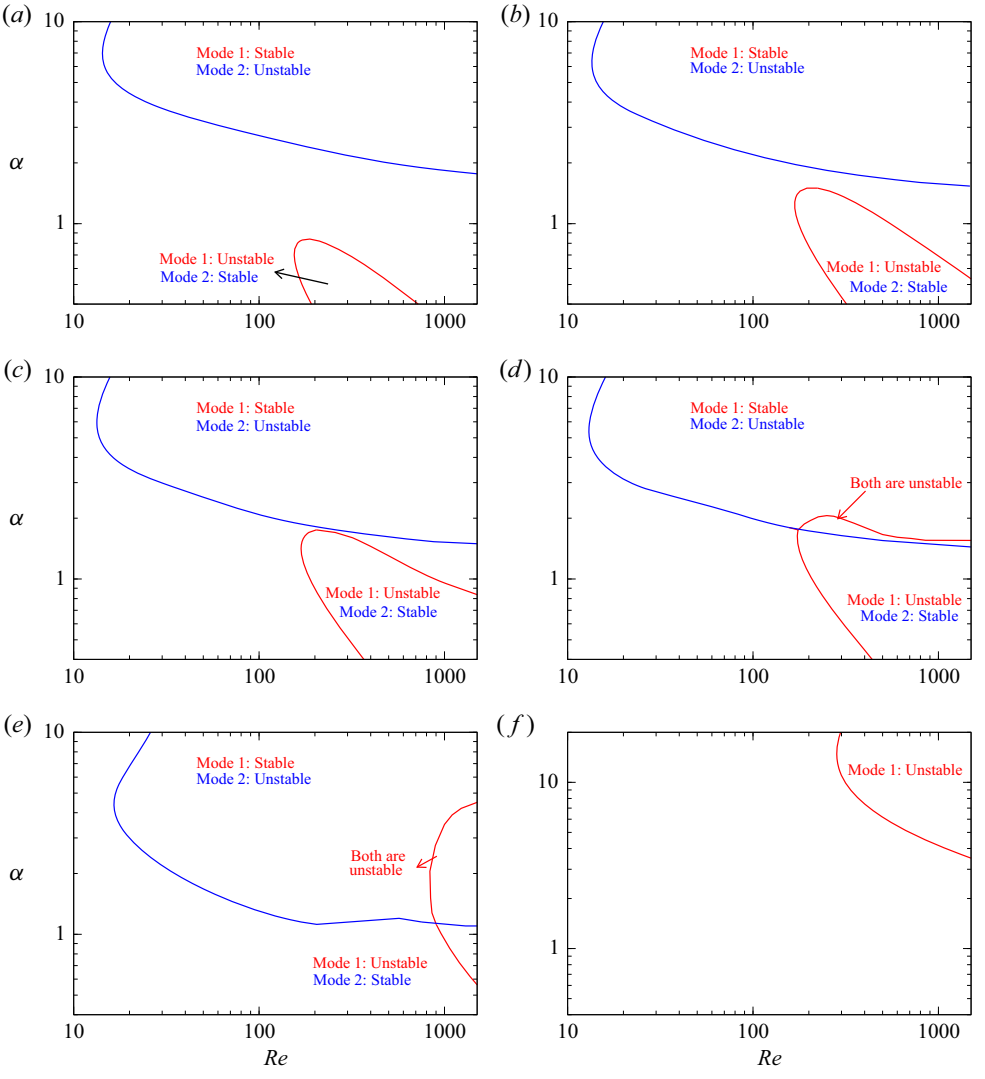


Figure 5. The neutral stability curves associated with the most unstable axisymmetric ($\beta = 0$) perturbation (excluding mode 'I') for different viscosity ratios in the immiscible configuration. (*a*) $\mu_r = 0.05$, (*b*) $\mu_r = 0.1$, (*c*) $\mu_r = 0.12$, (*d*) $\mu_r = 0.15$, (*e*) $\mu_r = 0.5$ and (*f*) $\mu_r = 0.95$. The rest of the parameters are $R_i = 0.7$, $\Gamma = 0$ and $\rho_r = 1$.

the neutral stability boundaries associated with mode '1' and mode '2' come closer and merge at $\mu_r \approx 0.12$. The overlap region (where both the modes are unstable) grows while the unstable region associated with mode 2 shrinks as we further increase the viscosity ratio, and it disappears for $\mu_r = 0.95$. Close inspection of figure 5(*a–f*) also reveals that the smallest Reynolds number for which either mode '1' or mode '2' is unstable increases with an increase in the viscosity ratio. In figures 6(*a*) and 6(*b*), the dispersion curves ($c_i/U_{max}$ vs $\alpha$) for different viscosity ratios are plotted for $Re = 100$ and $Re = 1500$, respectively. Other parameters are the same as those used to generate figure 5(*a–f*). In figure 6(*a*,*b*), it can be seen that $c_i/U_{max} > 0$ over a finite band of wavenumbers, indicating the presence of linear instability. Figure 6(*a*) shows that only mode '2' (in the large $\alpha$ region) is unstable

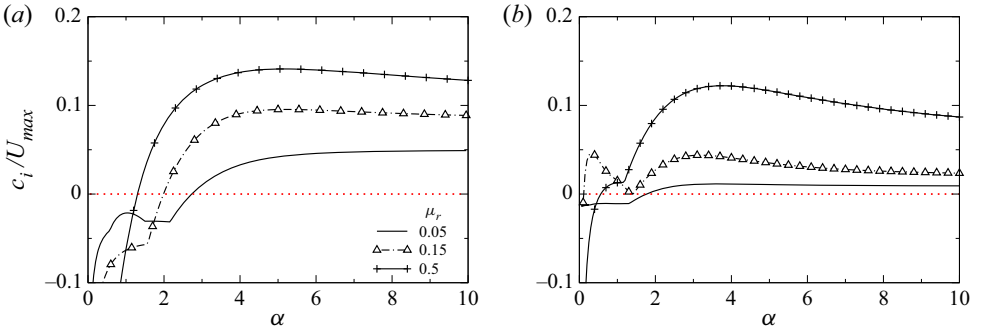


Figure 6. Effect of the viscosity ratio on the variation of $c_i/U_{max}$ vs $\alpha$ for (*a*) $Re = 100$ and (*b*) $Re = 1500$. Other parameters are $\beta = 0$, $\rho_r = 1$, $\Gamma = 0$ and $R_i = 0.7$.

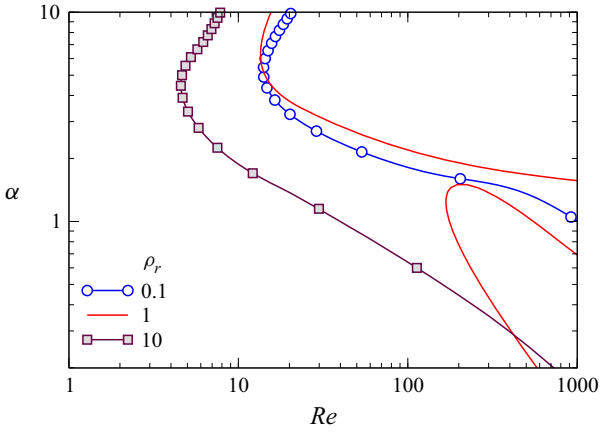


Figure 7. Effect of the density ratio on the neutral stability curve for $\mu_r = 0.1$ in the immiscible core-annular configuration. Other parameters are $\beta = 0$, $\Gamma = 0$ and $R_i = 0.7$.

for $Re = 100$, which can also be seen in the neutral stability curve plotted in figure 5. For $Re = 100$, it can be observed that the 'dominant' mode that corresponds to the value of $\alpha$ for which $c_i/U_{max}$ is maximum, decreases with increasing the viscosity ratio ($\mu_r$). In contrast, depending on the value of the viscosity ratio ($\mu_r$), mode '1' and/or mode '2' become the dominant mode for $Re = 1500$. It is also observed that the value of $\alpha$ associated with the dominant mode has a non-monotonic variation with $\mu_r$. In particular, inspection of figure 6(*b*) reveals the following: (i) only mode '2' (with large $\alpha$ value) is unstable for $\mu_r = 0.05$, (ii) for $\mu_r = 0.15$, mode '1' (with small $\alpha$ value) is the dominant mode as the value of $c_{i,max}/U_{max}$ is higher than that of mode '2' and (iii) mode '2' is the dominant mode for $\mu_r = 0.5$.

Then, the effect of the density ratio on the neutral stability curves is investigated for the axisymmetric perturbation ($\beta = 0$) in the immiscible configuration with $\mu_r = 0.1$ in figure 7. Other parameters are $\Gamma = 0$ and $R_i = 0.7$. It can be seen that the distinct modes merge and becomes a single unstable mode for $\rho_r = 0.1$ and 10. In order to find the range of the density ratios for which the two distinct modes are present, the variations of $c_i/U_{max}$ and $c_r/U_{max}$ with $\alpha$ are plotted for $\mu_r = 0.1$, $Re = 1000$, $\Gamma = 0$ and $R_i = 0.7$ in figures 8(*a*) and 8(*b*), respectively. It is observed that two unstable modes associated with low and high $\alpha$ values appear in the range $0.7 \leqslant \rho_r \leqslant 5$ for the set of

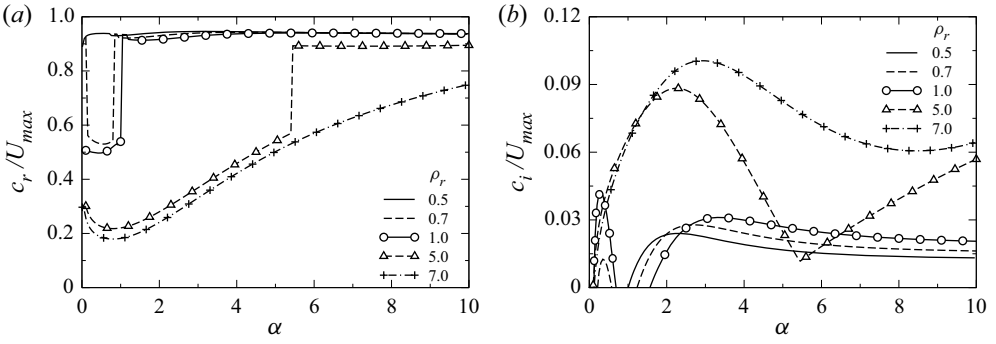


Figure 8. Variations of the normalised real ($c_r/U_{max}$) and imaginary ($c_i/U_{max}$) parts of the phase speed of the most unstable axisymmetric perturbation ($\beta = 0$); (*a*) $c_r/U_{max}$ vs $\alpha$ and (*b*) $c_i/U_{max}$ vs $\alpha$. Other parameters are $\mu_r = 0.1$, $Re = 1000$, $\Gamma = 0$ and $R_i = 0.7$.

parameters considered. Inspection of figures 8(*a*) and 8(*b*) reveals that for $\rho_r = 0.5$ and $\rho_r = 7$ there is only one unstable mode ($c_i/U_{max} > 0$).

### 3.1.2. *Corkscrew perturbation:* $\beta = 1$

After establishing the new mode of instability associated with the axisymmetric perturbation ($\beta = 0$), the linear stability behaviour of the corkscrew perturbation ($\beta = 1$) is investigated in this section. Figure 9(*a*) depicts the neutral stability curves associated with the most unstable mode (excluding mode 'I' with its real part, $c_{rI} = U_z|_{R_i}$) in the $(Re, \alpha)$-plane. The other parameters used to generate these results are $R_i = 0.7$, $\Gamma = 0$, $\rho_r = 1$ and $\mu_r = 1.2$. It can be seen that the corkscrew perturbation ($\beta = 1$) also exhibits two distinct unstable regions corresponding to the long (small $\alpha$) and short wavelengths (large $\alpha$) for the set of parameters considered. This is also clearly evident in figure 9(*b*), which presents the variations of the normalised real part of the phase speed ($c_r/U_{max}$) along the neutral stability boundaries. However, close inspection of figures 9(*a*) and 9(*b*) reveals that, in contrast to the axisymmetric perturbation ($\beta = 0$), the long- and short-wavelength unstable regions are associated with mode '2' (whose $c_r > c_{rI}$) and mode '1' (whose $c_r < c_{rI}$) in the case of the corkscrew perturbation ($\beta = 1$). The results for the corresponding miscible configuration (with $Sc = 1$, $q = 0.02$) is shown by the black dashed line in figures 9(*a*) and 9(*b*). It can be seen in figure 9(*a*) that the neutral stability curves for mode '2' (in the small $\alpha$ regime) in the immiscible configuration look similar to that of the single unstable TS mode observed in the miscible case. However, the critical Reynolds number associated with mode '2' in the immiscible configuration is much smaller than that of the TS mode in the miscible configuration.

The characteristics of modes '1' and '2' in the immiscible configuration for $\beta = 1$ are illustrated in figures 9(*c*) and 9(*d*), which show the eigenvalue spectra for two typical sets of parameters, namely ($Re = 3000$, $\alpha = 1$) and ($Re = 3000$, $\alpha = 6$) in the unstable long- and short-wavelength regions, respectively. In figure 9(*c*), it can be seen that the real part of the phase speed of the most unstable mode, $c_r$ is greater than $c_{rI}$; thus, it is mode '2' by definition. On the other hand, in figure 9(*d*), the phase speed of the most unstable mode, $c_r$ is less than $c_{rI}$; thus, it is mode '1' by definition.

The effect of the viscosity ratio for $\rho_r = 1$ and the density ratio for $\mu_r = 1.2$ on the neutral stability curve associated with the most unstable corkscrew ($\beta = 1$) perturbation (excluding mode 'I') in the immiscible configuration is investigated in figures 10(*a*) and

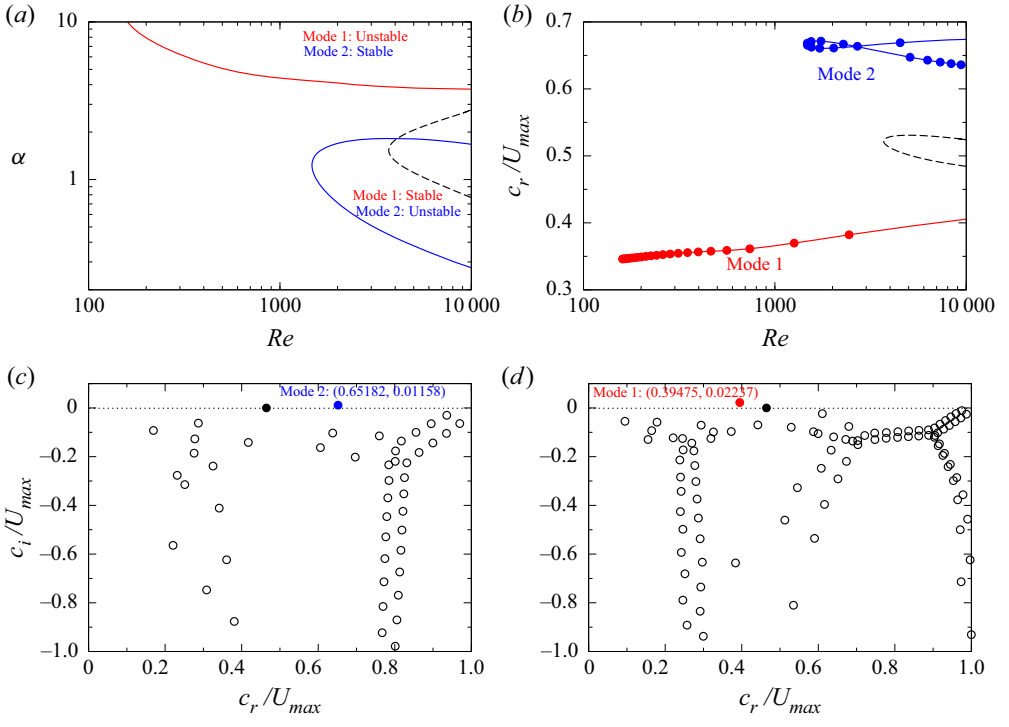


Figure 9. (*a*) The neutral stability curves for the most unstable corkscrew ($\beta = 1$) perturbation. (*b*) Variation of the real part of the phase speed of the most unstable mode as a function of *Re*. The result associated with a miscible configuration (with $Sc = 1$, $q = 0.02$) is shown by black dashed line in (*a*,*b*). The eigenvalue spectra for (*c*) $Re = 3000$, $\alpha = 1$ and (*d*) $Re = 3000$, $\alpha = 6$ in the immiscible configuration. Mode 'I' with $c_r = U_z|_{R_i} = 0.46448$ is shown by symbol (•) in (*c*,*d*). Other parameters are $R_i = 0.7$, $\Gamma = 0$, $\rho_r = 1$ and $\mu_r = 1.2$.

10(*b*), respectively. The other parameters are fixed at $\Gamma = 0$ and $R_i = 0.7$. The two distinct unstable regions for the long- and short-wavelength perturbations are apparent figure 10(*a*) for different viscosity ratios. Another important point to be noted here that, for $\mu_r = 1.5$, the neutral stability boundary in the long-wavelength region forms a closed loop. It can be seen in figure 10(*b*) that, while only mode '1' is unstable for low density ratios (see, for instance, $\rho_r = 0.1$), the two distinct unstable regions are present for $\rho_r \geqslant 0.5$. However, increasing the density ratio shifts the neutral boundary towards high Reynolds number for the set of parameters considered in figure 10(*b*). It is found (not shown) that all the neutral stability boundaries for mode '2' in figures 10(*a*) and 10(*b*) form close loops (albeit that this happens at large values of *Re*). This behaviour indicates that the unstable mode '2' in the interfacial configuration is not a TS mode. The new type of interfacial mode observed in this study for the immiscible core-annular configuration is similar to that found in two-layer Couette flow for a low viscosity ratio (Mohammadi & Smits 2017).

### 3.2. *Gas–liquid systems*

Finally, a parametric study is conducted to study the effect of the location of the interface ($R_i$) and the inverse capillary number ($\Gamma$) on the linear stability behaviour in gas–liquid systems. Two configurations, namely, (i) when the core fluid is a gas and the annular fluid is a liquid (i.e. $\rho_r = 10^3$ and $\mu_r = 10^2$) and (ii) when the core fluid is a liquid and the annular

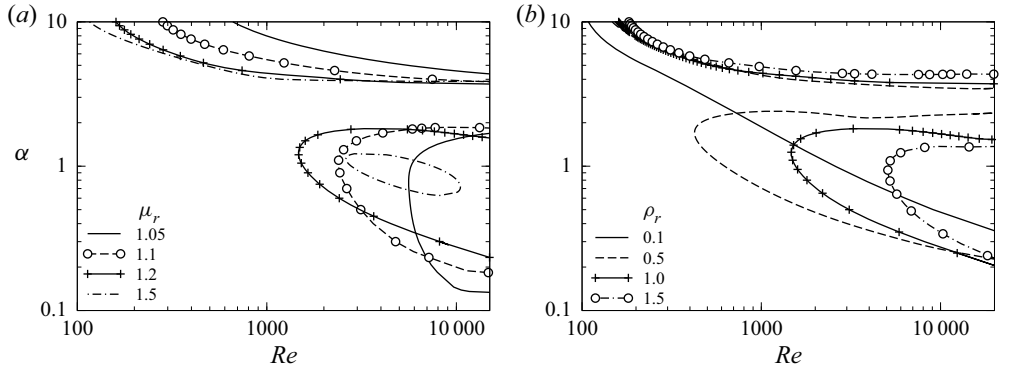


Figure 10. The neutral stability curves associated with the most unstable corkscrew ($\beta = 1$) perturbation (excluding mode 'I') for different (*a*) viscosity ratios for $\rho_r = 1$ and (*b*) density ratios for $\mu_r = 1.2$ in the immiscible configuration. Other parameters are $\Gamma = 0$ and $R_i = 0.7$.

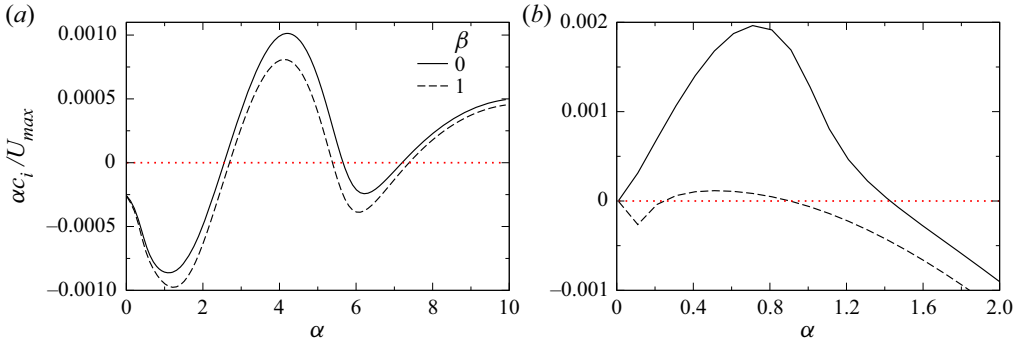


Figure 11. Effect of $\beta$ on the dispersion curves associated with the most unstable mode (excluding mode 'I'). (*a*) Core (gas)-annular (liquid) configuration ($\rho_r = 10^3$, $\mu_r = 10^2$). (*b*) Core (liquid)-annular (gas) configuration ($\rho_r = 10^{-3}$, $\mu_r = 10^{-2}$). Other parameters are $Re = 10^4$, $R_i = 0.7$ and $\Gamma = 0.1$.

fluid is a gas (i.e. $\rho_r = 10^{-3}$ and $\mu_r = 10^{-2}$) are considered. Figures 11(*a*) and 11(*b*) depict the dispersion curves ($\alpha c_i/U_{max}$ vs $\alpha$) associated with the most unstable axisymmetric ($\beta = 0$) and corkscrew ($\beta = 1$) perturbations (excluding 'I' mode) in gas–liquid systems for ($\rho_r = 10^3$, $\mu_r = 10^2$) and ($\rho_r = 10^{-3}$, $\mu_r = 10^{-2}$), respectively. It can be seen that, unlike the liquid–liquid system (discussed in § 3.1), the axisymmetric perturbation ($\beta = 0$) is the dominant mode in gas–liquid system. Thus, only the axisymmetric perturbation ($\beta = 0$) is examined hereafter in this section.

The effect of the interface location ($R_i$) and the inverse capillary number ($\Gamma$) on the dispersion curves for the most unstable mode (excluding mode 'I') are shown in figures 12(*a*) and 12(*b*) for $\beta = 0$, $\rho_r = 10^3$ and $\mu_r = 10^2$ (when the core fluid is a gas and the annular fluid is a liquid). The other parameters in figure 12(*a*) are $Re = 10^4$ and $\Gamma = 0.1$, and in figure 12(*b*) are $Re = 5000$ and $R_i = 0.7$. Increasing $R_i$ decreases the gradient of velocity in the annular region ($U'_{z,2}$) and decreases the centreline velocity to maintain the constant volumetric flow rate condition. Thus, increasing $R_i$ makes the flow in the annular region like a plug, which in turn stabilises the flow, as seen in figure 12(*a*). It can also be seen in figure 12(*a*) that the wavelength of the perturbation ($2\pi/\alpha$) associated with the highest growth rate decreases as the value of $R_i$ increases.

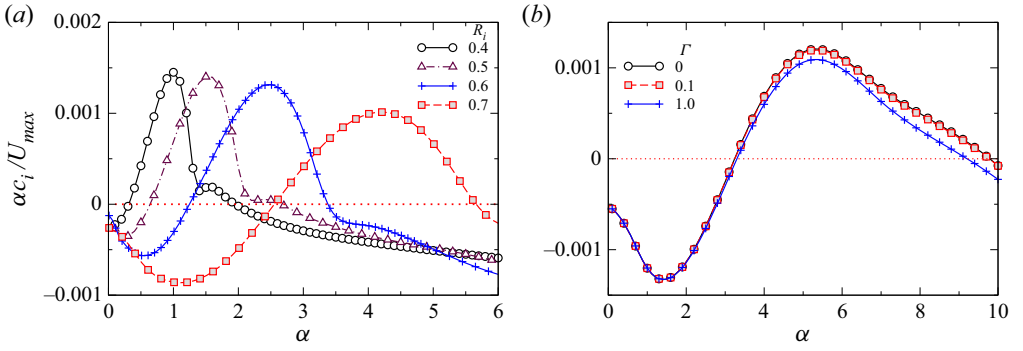


Figure 12. Dispersion curves associated with the most unstable mode (excluding mode 'I') for $\beta = 0$ (axisymmetric perturbation). (*a*) Effect of $R_i$ for $Re = 10^4$, $\Gamma = 0.1$ and (*b*) effect of $\Gamma$ for $Re = 5000$ and $R_i = 0.7$. The other parameters are $\rho_r = 10^3$ and $\mu_r = 10^2$.

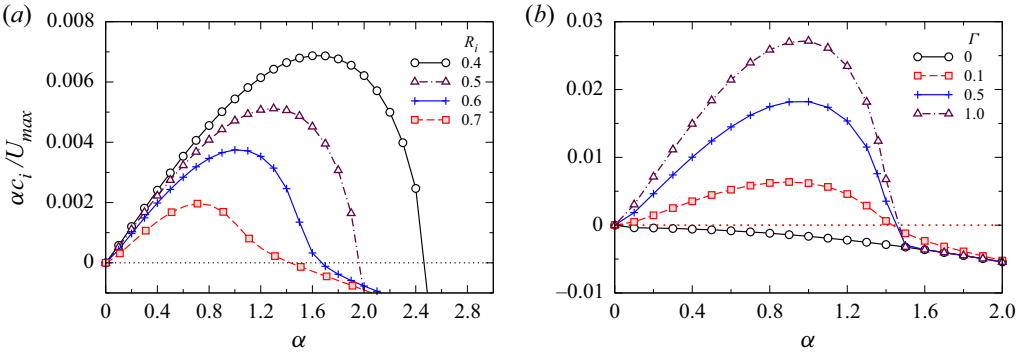


Figure 13. Dispersion curves associated with the most unstable mode (excluding mode 'I') for $\beta = 0$ (axisymmetric perturbation). (*a*) Effect of $R_i$ for $Re = 10^4$, $\Gamma = 0.1$ and (*b*) effect of $\Gamma$ for $Re = 2000$ and $R_i = 0.7$. The other parameters are $\rho_r = 10^{-3}$ and $\mu_r = 10^{-2}$.

It can be seen in figure 12(*b*) that increasing $\Gamma$, which corresponds to increasing the surface tension, stabilises the short-wave (high $\alpha$) perturbation.

Figures 13(*a*) and 13(*b*) depict the effect of the interface location ($R_i$) for $Re = 10^4$, $\Gamma = 0.1$ and the inverse capillary number ($\Gamma$) for $Re = 2000$, $R_i = 0.7$ on the growth rate of the perturbation for $\rho_r = 10^{-3}$ and $\mu_r = 10^{-2}$. In this case, as the core is a liquid (highly viscous as compared with gas), the plug flow region appears in the core layer, which stabilises the flow. In other words, increasing $R_i$ decreases the maximum growth rate of the perturbation (figure 13*a*). In the case of visco-plastic fluid flow in a channel, Frigaard (2001) also found that the presence of unyielded (plug) region highly stabilises the flow. It is found that increasing $\Gamma$ destabilises the long-wave perturbation (figure 12*b*). Thus, it can be concluded that increasing $\Gamma$, which corresponds to increasing the surface tension, stabilises the short-wave (high $\alpha$) but destabilises the long-wave perturbations (low $\alpha$) via the Rayleigh–Plateau instability. It is also observed (not shown) that the effect of $\Gamma$ on the stability characteristic is similar in the liquid–liquid configuration described in § 3.1.

## 4. Conclusions

The linear stability behaviour of the axisymmetric ($\beta = 0$) and corkscrew ($\beta = 1$) perturbations in the core-annular pressure-driven flow of two immiscible fluids in a cylindrical pipe is examined and compared to that observed in the corresponding configuration of two miscible fluids. The effects of the viscosity ratio ($\mu_r$), the density ratio ($\rho_r$), the Reynolds number ($Re$), the dimensionless interface location ($R_i$) and the inverse capillary number ($\Gamma$) have been investigated. Both liquid–liquid and gas–liquid systems are considered. A new mode of instability distinct from the TS mode and Yih's interface mode (Yih 1967) is discovered for a certain range of viscosity and density ratios in the immiscible liquid–liquid system ($\rho_r = O(1)$). The corkscrew perturbation also exhibits the new mode of instability for a certain range of density ratios. Contrary to the immiscible core-annular configuration, in which two regions of instability are observed for a range of viscosity and density ratios, only one mode is found to be unstable in the miscible core-annular flow. The new interfacial mode observed in the present study is similar to that found in two-layer Couette flow for low viscosity ratios (Mohammadi & Smits 2017). It is also observed that in the liquid–liquid systems ($\rho_r = O(1)$), while the corkscrew perturbation is dominant when the annular fluid is less viscous than the core fluid, the axisymmetric perturbation becomes more unstable when the annular fluid is more viscous than the core fluid. In contrast to the liquid–liquid system, the axisymmetric perturbation is always the dominant one in the gas–liquid system. It is found that increasing the interface radius stabilises the flow due to the presence of a plug flow region.

**Acknowledgements.** Professor S. Dey (IIT Kharagpur) encouraged me to investigate this problem. I also thank Dr S. Balusamy (IIT Hyderabad) for helping me to plot the graphical abstract. The anonymous reviewers are thanked for their valuable suggestions that have significantly improved the readability of the manuscript.

**Funding.** The author thanks the Science & Engineering Research Board, India for their financial support (grant number: MTR/2017/000029).

**Declaration of interests.** The author reports no conflict of interest.

**Author ORCIDs.**
Kirti Chandra Sahu https://orcid.org/0000-0002-7357-1141.

## Appendix A. Miscible core-annular configuration

In order to compare the linear stability behaviour of the immiscible configuration with the corresponding miscible system, the basic state and the linear stability equations associated with the core-annular flow of two miscible fluids are discussed briefly in this section. The reader is referred to Sahu (2016) for more details. The schematic diagram of the pressure-driven core-annular miscible flow configuration is shown in figure 14. In this configuration, the fluids are miscible and separated by a mixed region of thickness $q_0$ in region $R_0 - q_0/2 \leqslant r \leqslant R_0 + q_0/2$ of the pipe. The dimensionless dynamic viscosity is given by

$$\mu_0 = \exp(s_0 \ln \mu_r), \tag{A1}$$

where $s_0$ is given by

$$\left.\begin{aligned} s_0 &= 0, \quad 0 \leqslant r \leqslant R_i - q/2, \\ s_0 &= \sum_{i=1}^{6} a_i r^{i-1}, \quad R_i - q/2 \leqslant r \leqslant R_i + q/2, \\ s_0 &= 1, \quad R_i + q/2 \leqslant r \leqslant 1, \end{aligned}\right\} \tag{A2}$$

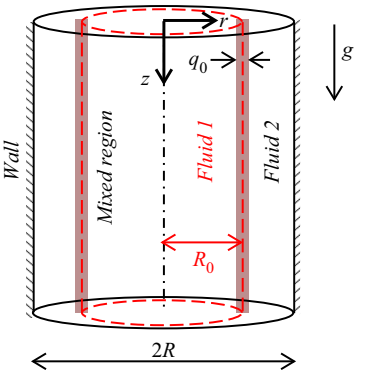


Figure 14. Schematic of the pressure-driven core-annular flows of two miscible fluids in a vertical pipe of radius $R$. The acceleration due to gravity, $g$ acts in the positive $z-$direction. The fluids are separated by a mixed region of thickness $q_0$ occupying the region $R_0 - q_0/2 \leqslant r \leqslant R_0 + q_0/2$.

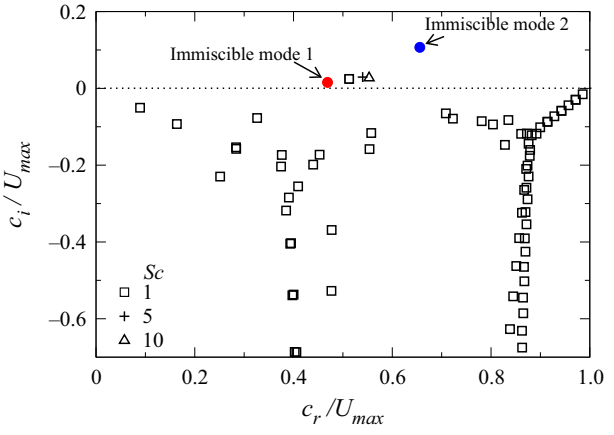


Figure 15. Effect of $Sc$ on the most unstable mode in the miscible core-annular flow configuration for $Re = 1500$, $\alpha = 2.5$, $\beta = 0$, $q = 0.02$, $\mu_r = 0.5$, $R_i = 0.7$ and $\rho_r = 1$. The complete eigenvalue spectrum corresponds to $Sc = 1$. The unstable modes '1' and '2' in the corresponding immiscible configuration with $\Gamma = 0$ are shown by ('$\circ$', red) and ('$\circ$', blue), respectively. It can be seen that increasing $Sc$ has a non-monotonic effect on the growth rate of the most unstable mode in the miscible configuration.

where $a_i$ $(i = 1, 6)$ are obtained by assuming that the scalar is continuous up to the second derivative at $r = R_i - q/2$ and $r = R_i + q/2$ (Govindarajan 2004; Sahu & Govindarajan 2011), wherein $q = q_0/R$. The other variables are non-dimensionalised in the same manner as described in § 2.1 for the immiscible configuration. When the Péclet number $Pe(\equiv ReSc)$ is large, $s_0$ could be approximated by an error function that depends on the combination $(r - R_i)\sqrt{Pe/z}$. In the stability calculation, the dependence of $s_0$ on $z$ is neglected. This 'quasi-steady' approximation to represent basic concentration profile in miscible flows is justified if the wavelength $2\pi/\alpha$ of the disturbance is much shorter than the length scale over which $s_0$ varies with $z$, namely $q^2Pe$. It is also to be noted here that, after Tan & Homsy (1986), several authors have used the quasi-steady approximation to represent basic concentration profile in miscible flows in the form of a hyperbolic tangent (Ern *et al.* 2003), an error function (Selvam *et al.* 2007; Talon & Meiburg 2011) and a fifth-order polynomial (Ranganathan & Govindarajan 2001; Sahu 2016).

In the case of the miscible core-annular flow, the basic state is given by

$$\frac{1}{r}\frac{\partial}{\partial r}\left[r\mu_0\frac{\partial U_z}{\partial r}\right] = \frac{\mathrm{d}P}{\mathrm{d}z}Re, \tag{A3}$$

which is solved using the no-slip boundary condition at the pipe wall and the symmetric boundary condition at the centreline of the pipe. Unlike the immiscible configuration, the interfacial boundary conditions are not needed in this case as the dynamics is characterised by the diffusion coefficient ($\mathcal{D}$) of the scalar and not the interfacial tension (no sharp interface). The dimensionless pressure gradient, $\mathrm{d}P/\mathrm{d}z$ is obtained using constant volumetric flow condition.

In the derivation of the linear stability equations for the miscible configuration, the scalar variable can be expressed as $s_0(r) + s(r)\exp(\mathrm{i}(\alpha z + \beta\theta - \alpha ct))$, such that the amplitude of the perturbation viscosity, $\mu = (\partial\mu_0/\partial s_0)s$. The normal mode analysis used in this case is also similar to that given in § 2.1.2. The linear stability equations for the miscible configuration are given by

$$u_r' + \frac{u_r}{r} + \frac{\beta u_\theta}{r} + \alpha u_z = 0, \tag{A4}$$

$$\rho(-\alpha c u_r + \alpha u_r U_z) = p' - \frac{\mathrm{i}}{Re}\left[\mu_0\left\{u_r'' + \frac{u_r'}{r} - \left(\frac{\beta^2+1}{r^2} + \alpha^2\right)u_r - \frac{2\beta}{r^2}u_\theta\right\} + 2\mu_0' u_r' + \alpha U_z'\mu\right], \tag{A5}$$

$$\rho(-\alpha c u_\theta + \alpha u_\theta U_z) = -\frac{\beta p}{r} - \frac{\mathrm{i}\mu_0}{Re}\left\{u_\theta'' + \frac{u_\theta'}{r} - \left(\frac{\beta^2+1}{r^2} + \alpha^2\right)u_\theta - \frac{2\beta}{r^2}u_r\right\} - \frac{\mathrm{i}\mu_0'}{Re}\left[u_\theta' - \frac{u_\theta}{r} - \frac{\beta u_r}{r}\right], \tag{A6}$$

$$\rho(-\alpha c u_z + U_z' u_r + \alpha U_z u_z) = -\alpha p - \frac{\mathrm{i}\mu_0}{Re}\left\{u_z'' + \frac{u_z'}{r} - \left(\frac{\beta^2}{r^2} + \alpha^2\right)u_z\right\} - \frac{\mathrm{i}\mu_0'}{Re}\left[v_z' - \alpha v_r\right] - \frac{\mathrm{i}U_z'}{Re}\mu' - \frac{\mathrm{i}\mu}{Re}\left[U_z'' + \frac{U_z'}{r}\right], \tag{A7}$$

$$-\alpha c s + s_0' u_r + \alpha U_z s = -\frac{\mathrm{i}}{ReSc}\left\{s'' + \frac{s'}{r} - \left(\frac{\beta^2}{r^2} + \alpha^2\right)s\right\}. \tag{A8}$$

Here, $\rho = s_0\rho_r + (1 - s_0)$ and $Sc(\equiv \mu_1/\rho\mathcal{D})$ is the Schmidt number. It is noted here that (A4)–(A7) are similar to the stability equations for each layer in the case of immiscible core-annular flow configuration (§ 2.1.2). The boundary conditions for the perturbation velocity field $(v_r, v_\theta, v_z)$ at the centreline and wall of the pipe are the same as (2.10) and (2.13*a–c*). The boundary conditions for the scalar variable, $s$ are $s = 0$ and $s' = 0$ at the centreline and wall of the pipe, respectively. For more details and validation of the stability analysis of the miscible configuration presented in this section, the reader is referred to our previous studies Sahu & Govindarajan (2011), Sahu (2016, 2019).

## Appendix B. Grid convergence test

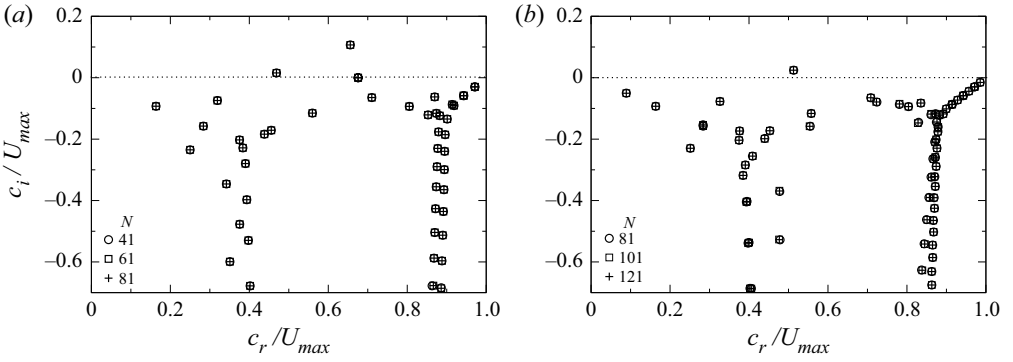


Figure 16. The eigenvalue spectra obtained using different numbers of grids ($N$) in the ($a$) immiscible configuration (figure 1) with $\Gamma = 0$ and ($b$) miscible configuration (figure 14) with $Sc = 1$ and $q = 0.02$. The other parameters are $Re = 1500$, $\alpha = 2.5$, $\beta = 0$, $R_i = 0.7$, $\mu_r = 0.5$ and $\rho_r = 1$.

## References


Boomkamp, P.A.M. & Miesen, R.H.M. 1996 Classification of instabilities in parallel two-phase flow. *Int. J. Multiphase Flow* **22**, 67–88.

Canuto, C., Hussaini, M.Y., Quarteroni, A. & Zang, T.A. 1987 *Spectral Methods in Fluid Dynamics*, 1st edn. Springer.

Cao, Q., Ventresca, L., Sreenivas, K.R. & Prasad, A.K. 2003 Instability due to viscosity stratification downstream of a centreline injector. *Can. J. Chem. Engng* **81**, 913–922.

Ern, P., Charru, F. & Luchini, P. 2003 Stability analysis of a shear flow with strongly stratified viscosity. *J. Fluid Mech.* **496**, 295–312.

Frigaard, I.A. 2001 Super-stable parallel flows of multiple visco-plastic fluids. *J. Non-Newtonian Fluid Mech.* **100**, 49–76.

Govindarajan, R 2004 Effect of miscibility on the linear instability of two-fluid channel flow. *Int. J. Multiphase Flow* **30**, 1177–1192.

Govindarajan, R. & Sahu, K.C. 2014 Instabilities in viscosity-stratified flows. *Annu. Rev. Fluid Mech.* **46**, 331–353.

Hickox, C.E. 1971 Instability due to viscosity and density stratification in axisymmetric pipe flow. *Phys. Fluids* **14**, 251–262.

Hinch, E.J. 1984 A note on the mechanism of the instability at the interface between two shearing fluids. *J. Fluid Mech.* **144**, 463–465.

Hooper, A.P. 1985 Long-wave instability at the interface between two viscous fluids: thin layer effects. *Phys. Fluids* **28** (6), 1613–1618.

Hooper, A.P. & Boyd, W.G.C. 1983 Shear flow instability at the interface between two fluids. *J. Fluid Mech.* **128**, 507–528.

Hu, H.H. & Joseph, D.D. 1989 Lubricated pipelining: stability of core-annular flows. Part 2. *J. Fluid Mech.* **205**, 359–396.

Joseph, D.D., Bai, R., Chen, K.P. & Renardy, Y.Y. 1997 Core-annular flows. *Annu. Rev. Fluid Mech.* **29**, 65–90.

Joseph, D.D., Renardy, M. & Renardy, Y.Y. 1984 Instability of the flow of two immiscible liquids with different viscosities in a pipe. *J. Fluid Mech.* **141**, 309–317.

Malik, S.V. & Hooper, A.P. 2005 Linear stability and energy growth of viscosity stratified flows. *Phys. Fluids* **17**, 024101.

Mohammadi, A. & Smits, A.J. 2017 Linear stability of two-layer Couette flows. *J. Fluid Mech.* **826**, 128–157.

Orazzo, A., Coppola, G. & De Luca, L. 2014 Disturbance energy growth in core-annular flow. *J. Fluid Mech.* **747**, 44–72.

RANGANATHAN, B.T. & GOVINDARAJAN, R. 2001 Stabilisation and destabilisation of channel flow by location of viscosity-stratified fluid layer. *Phys. Fluids* **13** (1), 1–3.
REDAPANGU, P.R., SAHU, K.C. & VANKA, S.P. 2012 study of pressure-driven displacement flow of two immiscible liquids using a multiphase lattice Boltzmann approach. *Phys. Fluids* **24**, 102110.
SAFFMAN, P.G. & TAYLOR, G.I. 1958 The penetration of a finger into a porous medium in a Hele-Shaw cell containing a more viscous liquid. *Proc. R. Soc. Lond.* A **245**, 312–329.
SAHU, K.C. 2016 Double-diffusive instability in core–annular pipe flow. *J. Fluid Mech.* **789**, 830–855.
SAHU, K.C. 2019 Linear instability in a miscible core-annular flow of a Newtonian and a Bingham fluid. *J. Non-Newtonian Fluid Mech.* **264**, 159–169.
SAHU, K.C. & GOVINDARAJAN, R. 2011 Linear stability of double-diffusive two-fluid channel flow. *J. Fluid Mech.* **687**, 529–539.
SAHU, K.C. & GOVINDARAJAN, R. 2016 Linear stability analysis and direct numerical simulation of two-layer channel flow. *J. Fluid Mech.* **798**, 889–909.
SAHU, K.C. & MATAR, O.K. 2010 Three-dimensional linear instability in pressure-driven two-layer channel flow of a Newtonian and a Herschel–Bulkley fluid. *Phys. Fluids* **22**, 112103.
SAHU, K.C., VALLURI, P., SPELT, P.D.M. & MATAR, O.K. 2007 Linear instability of pressure-driven channel flow of a Newtonian and Herschel–Bulkley fluid. *Phys. Fluids* **19**, 122101.
SALIN, D. & TALON, L. 2019 Revisiting the linear stability analysis and absolute–convective transition of two fluid core annular flow. *J. Fluid Mech.* **865**, 743–761.
SCHMID, P.J. & HENNINGSON, D.S. 2001 *Stability and transition in shear flows*. Springer-Verlag New York, Inc.
SCOFFONI, J., LAJEUNESSE, E. & HOMSY, G.M. 2001 Interface instabilities during displacement of two miscible fluids in a vertical pipe. *Phys. Fluids* **13**, 553–556.
SELVAM, B., MERK, S., GOVINDARAJAN, R. & MEIBURG, E. 2007 Stability of miscible core-annular flows with viscosity stratification. *J. Fluid Mech.* **592**, 23–49.
SELVAM, B., TALON, L., LESSHAFFT, L. & MEIBURG, E. 2009 Convective/absolute instability in miscible core-annular flow. Part 2. Numerical simulations and nonlinear global modes. *J. Fluid Mech.* **618**, 323–348.
TALON, L. & MEIBURG, E. 2011 Plane Poiseuille flow of miscible layers with different viscosities: instabilities in the Stokes flow regime. *J. Fluid Mech.* **686**, 484–506.
TAN, C.T. & HOMSY, G.M. 1986 Stability of miscible displacements: rectangular flow. *Phys. Fluids* **29**, 3549–3556.
USHA, R. & SAHU, K.C. 2019 Interfacial instability in pressure-driven core-annular pipe flow of a Newtonian and a Herschel–Bulkley fluid. *J. Non-Newtonian Fluid Mech.* **271**, 104144.
VALLURI, P., NARAIGH, L.O., DING, H. & SPELT, P.D.M. 2010 Linear and nonlinear spatio-temporal instability in laminar two-layer flows. *J. Fluid Mech.* **656**, 458–480.
WEINSTEIN, S.J & RUSCHAK, K.J. 2004 Coating flows. *Annu. Rev. Fluid Mech.* **36**, 29–53.
YIANTSIOS, S.G. & HIGGINS, B.G. 1988*a* Linear stability of plane Poiseuille flow of two superposed fluids. *Phys. Fluids* **31**, 3225–3238.
YIANTSIOS, S.G. & HIGGINS, B.G. 1988*b* Numerial solution of eigenvalue problems using the compound matrix-method. *J. Comput. Phys.* **74**, 25–40.
YIH, C.S. 1967 Instability due to viscous stratification. *J. Fluid Mech.* **27**, 337–352.
YIH, C.S 1990 Wave formation on a liquid layer for de-icing airplane wings. *J. Fluid Mech.* **212**, 41–53.